Voids and Superstructures:
correlations and induced large–scale velocity flows

Marcelo Lares⋆, Heliana E. Luparello, Victoria Maldonado, Andrés N. Ruiz, Dante J. Paz, Laura Ceccarelli, & Diego Garcia Lambas

Instituto de Astronomía Teórica y Experimental, CONICET-UNC, and Observatorio Astronómico de Córdoba, Argentina

ABSTRACT

The expanding complex pattern of filaments, walls and voids build the evolving cosmic web with material flowing from underdense onto high density regions. Here we explore the dynamical behaviour of voids and galaxies in void shells relative to neighboring overdense superstructures, using the Millenium Simulation and the main galaxy catalogue in Sloan Digital Sky Survey data. We define a correlation measure to estimate the tendency of voids to be located at a given distance from a superstructure. We find voids–in–clouds (S–types) preferentially located closer to superstructures than voids–in–voids (R–types) although we obtain that voids within $\sim 40h^{-1}$ Mpc of superstructures are infalling in a similar fashion independently of void type. Galaxies residing in void shells show infall towards the closest superstructure, along with the void global motion, with a differential velocity component depending on their relative position in the shell with respect to the direction to the superstructure. This effect is produced by void expansion and therefore is stronger for R–types. We also find that galaxies in void shells facing the superstrucure flow towards the overdensities faster than galaxies elsewere at the same relative distance to the superstructure. The results obtained for the simulation are also reproduced for the SDSS data with a linearized velocity field implementation.

Key words: large scale structure of Universe – cosmology: observations – methods: statistics – data analysis

1 MOTIVATION

The cosmic web is the largest scale outcome of the anisotropic growth of mass overdensities. It also represents the transition between the linear and non-linear regimes and encodes information about the early phases of structure formation. The analysis of the mass transport between different environments clearly shows how matter flows from voids into walls, and then via filaments into cluster regions, which form the nodes of the cosmic web (see e.g. Van de Weygaert & Platen 2011; Cautun et al. 2014), producing different redshift evolution of haloes in different environments (Hahn et al. 2007).

The relations between the different types of the largest structures in the universe have been suggested on several contexts (Einasto et al. 1986, 1997; Platen et al. 2008; Aragón-Calvo et al. 2010; Einasto et al. 2011). This allows to analyse the large–scale structure in terms of the large overdense structures, or alternatively in terms of the large underdense regions. Actually, the largest overdense structures that shape the cosmic web, also serve as boundaries for voids (Cautun et al. 2014). Also, by understanding the evolutionary processes of the different structures we can obtain a

deeper insight on the origin and history of the present structure (Leclercq et al. 2015).

In order to deepen our understanding on the nature of voids and the evolution of their properties it is crucial to take into account the surrounding environment where they are embedded (Paranjape et al. 2012). Essentially, the hierarchy of voids arises by the assembly of mass in the growing nearby structures. Sheth & van de Weygaert (2004) suggest that while some voids remain as underdense regions, other voids fall in on themselves due to the collapse of dense structures surrounding them. According to this scenario, void evolution exhibits two opposite processes, expansion and collapse, being the dominant process determined by the global density around the voids. The distinction between these two types of void behaviour depends on the surrounding environment. It is expected that the large underdense regions with surrounding overdense shells will undergo a *void-in-cloud* evolution mode. These voids are likely to be squeezed as the surrounding structures tend to collapse onto them. On the other hand, voids in an environment more similar to the global background density will expand and remain as underdense regions following a so called *void-in-void* mode. In a series of works (Ceccarelli et al. 2013; Paz et al. 2013; Ruiz et al. 2015) we have considered an alternative classification of void according to their environment taking into account the cumulative radial den-
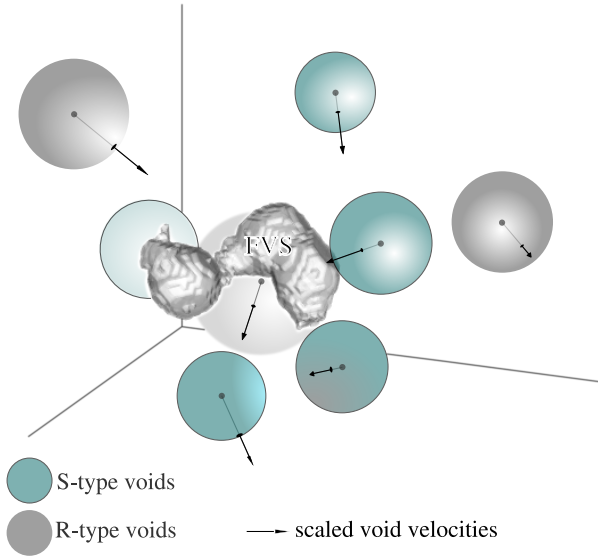
Figure 1. A Visualization of a group of void–FVS pairs, including all the voids (represented as spheres) that have the FVS (in the center of the Figure) as their closest one. Arrows are scaled representations of the void velocity vector, with dotted segments located inside or behind voids. This example corresponds to a subset of data from the simulation. Other FVSs and voids in the neighbourhood are not shown for simplicity. Darker spheres represent R–type voids and delineated spheres represent S–type voids. The latest are typically closer and moving towards the FVS.

sity profiles. Voids with a surrounding overdense shell exhibit a rising cumulative density profile, which overcompensates the underdensity and therefore reach possitive values between 2 and 3 times the void radius. These voids, dubbed S–type after its shell–like structure, are likely collapsing. On the other hand, voids with a smoothly rising integrated density profile that approaches the mean density at large distances (hereafter R–type voids) show a continuos expansion. In this scheme, R-type voids resemble void-in-void objects while void in clouds are consistent with the S-type definition.

The origin of the large–scale flows observed in the local Universe has been subject of controversy during the last decades. While several works have focused on the search of a great attractor consistent with peculiar velocities of local structures, an alternative approach includes the expansion of the local void as proposed by Tully et al. (2008, 2014). Albeit the contribution of the local void dynamics improves the description of the velocity fields in the nearby Universe, the estimated peculiar velocity of the local group is still conflicting with that predicted from the infall onto the Shapley supecluster and the local void expansion, due to the presence of residual velocities of ∼ 200 km/s for the local group (van de Weygaert 2016, and references therein).

In recent works we have reported the non-negligible motions of voids as a whole (Ceccarelli et al. 2016; Lambas et al. 2016), adding a new component affecting galaxy peculiar velocities. These global motions can be a key piece to complete the scenario of the dynamics of local structures. In this work we show that the velocities generated by the mass under/over densities associated with the large–scale structures of the galaxy distribution are complementary to obtain a detailed description of the large–scale velocity flows. In this context, we study the joint dynamics of galaxies with respect
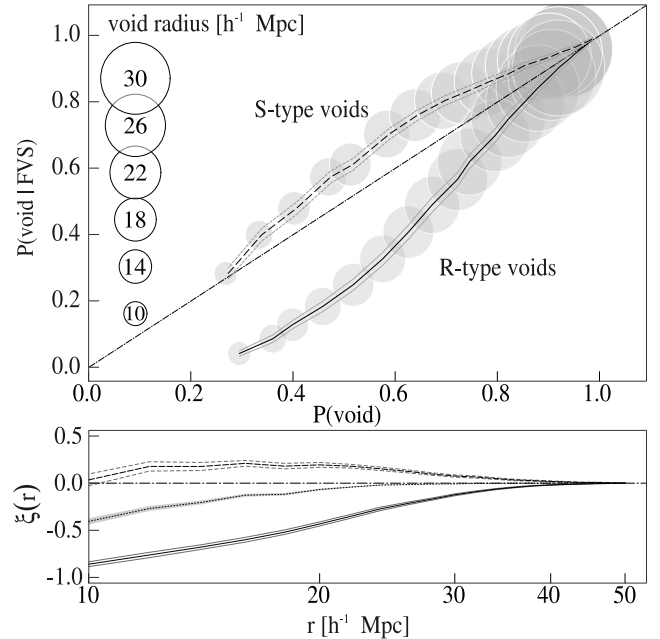

Figure 2. Spatial distribution of voids with respect to FVSs, in the simulation. *Upper panel:* The curves show the conditional probability, $P(void|FVS)$, of finding a randomly placed sphere containing simultaneously void and FVS volume fractions, as a function of the probability $P(void)$ that the sphere contains a fraction of void volume, in spite of the presence of FVS. If the locations of voids and FVSs were independent, $P(void|FVS) \simeq P(void)$ for any value of sphere radius (dot–dashed line indicating a one–to–one relation). The upper curve corresponds to the results for S–type voids, and the lower curve to R–type voids. Circle radii scale linearly with the radius of the random spheres. Uncertainties are computed using Jackknife resamplings. *Bottom panel:* Void–FVS correlation function $\xi(r)$. We use the definition of $\xi(r) - \xi_{\text{void–FVS}}(r)$ given in Eq. 4. S–type voids exhibit a positive correlation in a wide range of scales, consistent with their denser environment. On the other hand, R–type voids and FVSs are anticorrelated, with a stronger signal than that of S–type voids. The central curve corresponds to the full sample of voids, without separating by type.

to voids and Future Virialized Structures (hereafter FVSs), in order to explore coherent patterns of motions of mass from the shells of voids to the largest overdensities.

In the next section, we describe the general methods used to identify voids and FVSs, both in semianalytic galaxies and in an observational galaxy catalogue. Then, in Sec. 3 we analyse the spatial distribution of voids relative to superstructures and their associated dynamics. The same analysis is then performed to galaxies, where their motions are considered separately for different configurations of relative positions of galaxies, voids and FVSs. In Sec. 4 we also present similar studies applied to observational data. Finally, we present a discussion of our results in the context of recent works in Sec. 5.

2 DATA

2.1 Galaxy catalogues

The observational galaxies used in this work correspond to the Main Galaxy Sample of the Sloan Digital Sky Survey Data Release 7 (SDSS-DR7, Abazajian et al. 2009). This catalogue comprises almost a million of spectroscopic galaxies with redshift measure-

ments up to $z \leqslant 0.3$ and an upper apparent magnitude limit of 17.77 in the *r*-band. From this sample we select galaxies with a limiting redshift $z = 0.12$ and a maximum absolute magnitude in the *r*-band of $M_r - 5\log_{10}(h) = -19.95$, in order to obtain a volume complete sample of galaxies at that redshift. The limits of this sample are chosen on the basis of a compromise between the volume and the number of tracers. For SDSS velocities, we adopt the peculiar velocity field presented by Wang et al. (2012). The authors used the linear theory connection between mass overdensity and peculiar velocity to reconstruct the 3D peculiar velocity field of SDSS galaxies (Wang et al. 2009). With this velocity field we compute the bulk void velocities in the SDSS sample. For an analysis of the effects of using linearised velocities, we refer the reader to the Appendix of Ceccarelli et al. (2016). We also analysed the influence of large–scale flows in observational data. For this purpose we used a galaxy group catalogue which follows the identification method presented in Yang et al. (2005), applied to SDSS-DR4 in Yang et al. (2007), and updated by the authors to the SDSS-DR7[1]. For this sample of groups, we also adopted the linearized velocity field by Wang et al. (2012).

On the other hand, the simulated galaxies used were extracted from a semi-analytical model of galaxy formation (SAM) applied to the Millennium Simulation (MS, Springel et al. 2005), a cosmological *N*-body simulation which counts with 2140^3 dark matter particles evolved in a cubic comoving box of $500h^{-1}$ Mpc on a side. The cosmological parameters adopted for the MS correspond to *WMAP*1 results (Spergel et al. 2003), i.e. a flat Λ cold dark matter cosmology with $\Omega_m = 0.25$, $\Omega_\Lambda = 0.75$, $\Omega_b = 0.045$, $\sigma_8 = 0.9$, $h = 0.73$ and $n = 1.0$. Given that the MS is a dark matter only simulation, their dark matter haloes needs to be populated with a SAM to obtain a galaxy population. In this work we use the public catalogue developed by Guo et al. (2011), which is available at the Millennium Database[2]. In order to make a fair comparison between observations and simulated data for the complete simulated galaxy population, we select a sample with the same number density than the observations This was achieved by selecting all galaxies brighter than $M_r - 5\log h = -20.6$, which guarantees the volume density required. Althought this threshold in absolute magnitude is not the same than the limiting magnitude used to define the volume–limited sample of galaxies, it reproduces satisfactorily the distribution of galaxies. (see e.g. Contreras et al. 2013, 2015). The difference between the two values arises from the fact that semianalytical models does not reproduce exactly the luminosity function of galaxies in SDSS.

2.2 Catalogues of cosmic voids

To construct the void catalogue we follow the procedure described in Ruiz et al. (2015), which is a modified version of the algorithms presented in Padilla et al. (2005) and Ceccarelli et al. (2006). The galaxies (either simulated or observed) are the tracers of the density field used in void the identification. The method starts with a contrast density field estimation performed with a Voronoi tessellation, where underdense cells are selected as void candidates. Centred in those positions, we compute the integrated density contrast $\Delta(r)$ at increasing values of radius r, selecting as void candidate the largest spheres which satisfy the condition $\Delta(R_{\text{void}}) < -0.9$ and defining R_{void} as the void radius. Afterwards, the centre position of
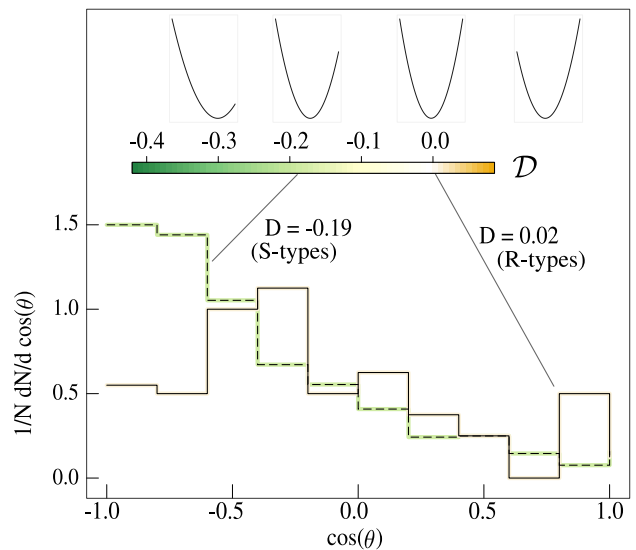
---

[1] http://gax.shao.ac.cn/data/Group.html
[2] http://gavo.mpa-garching.mpg.de/Millennium

Figure 3. Normalized histograms of the distribution of $\cos(\theta)$, where θ is the angle between the relative velocity and the relative position of the void–FVS system (see text for details); for subsamples of R–type voids (dotted line) and for S–type voids (solid line) in the simulation. These subsamples were chosen in order to show the different values of $\mathcal{D}$. One sample comprises R–type voids with a separation from the FVS greater than $d>40h^{-1}$ Mpc, and $M<10^{14}h^{-1}$ $M_\odot$. The sample of S–type voids is restricted to $d<40h^{-1}$ Mpc, and $M>10^{14.2}h^{-1}$ $M_\odot$. On the top of the figure, we show a scale indicating the values of the dipole coefficient $\mathcal{D}$ for both samples. We also show, for reference, model distributions for different values of the dipole coefficient (-0.4, -0.2, 0, and 0.2, respectively).

void candidates are randomly tilted and the sphere is allowed to grow in order to recentre the void. Finally, a void of radius R_{void} is selected as the largest sphere satisfying the underdense condition and not overlapping with any other underdense sphere. The final catalogues comprises 1676 voids for the full Millennium box and 495 voids for the total SDSS sample, but for dynamical analyses we used only 288 of them (121 R–type and 167 S–type), which belong to the inner region of the survey where the velocity field of Wang et al. (2012) has a reliable reconstruction. The void radii are in the range 8-26 h^{-1} Mpc, both in SDSS and the simulation.

2.3 Catalogues of superstructures

In previous works, we have defined the procedures to select superstructures that will be virialized systems in the distant future (Luparello et al. 2011). The criteria applied can be used to both observational and simulated galaxy catalogues. The method relies on the computation of the luminosity density field, by convolving the spatial distribution of galaxies (either observed or SAM) with a kernel function weighted by galaxy luminosity. We adopted an Epanechnikov kernel of $8h^{-1}$ Mpc to sample the density field into a grid composed by cubes of $1h^{-1}$ Mpc side. We then select the highest luminosity density groups of cells to isolate the large structures that will become virialized systems in the future (Dünner et al. 2006) In our final catalogue we identified 150 FVSs comprising 11394 galaxies in the SDSS, out of which 105 FVSs are within the region where we used the reconstructed velocity field data by Wang et al. (2012). The simulation, on the other hand, has 790 FVSs due to its larger volume, which is approximately 6 times the SDSS volume.

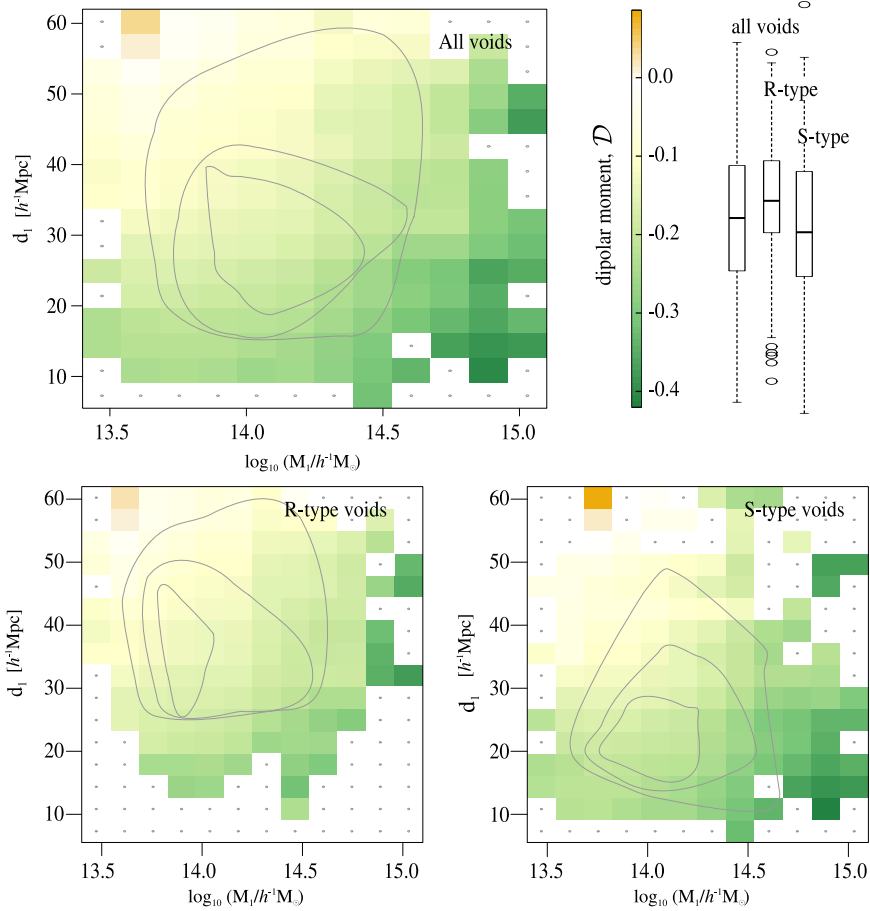**Figure 4.** Dependence of the dipole moment on FVS mass and void–FVS separation in the simulation data. We show 2D histograms of the dipole moment estimator $\mathcal{D}$ (encoded in color) for the distribution of $\cos(\theta)$ in bins of FVS mass and void–FVS distance. Positive values of $\cos(\theta)$ correspond to positive velocity components on the FVS–void direction (see text for its definition), which indicates that the void is moving away their closest FVS. We show in the upper panel the full sample of void–FVS pairs, and in the bottom left and right panels, R– and S–type voids, respectively. Box plots correspond to the distributions of $\mathcal{D}$ for each sample. Contour levels are shown for the number of objects contributing to the signal in each bin, and correspond to 25, 50 and 75 per cent of the pairs.

3   ANALYSIS IN THE SIMULATION DATA

Here we present the main results obtained from the analysis of voids and FVSs identified in the simulated galaxy catalogue. In what follows, we develop a measurement for the correlation between extended regions corresponding to voids and FVSs and analyse their associated dynamics.

3.1   Spatial distribution of voids relative to FVSs

The definition of voids and FVSs results in two types of structures that are distributed in space occupying somewhat complementary locations. In this context, it is worth asking if these structures are related in a non trivial fashion (i.e., if their distributions are consistent with a random distribution or if the locations of overdense structures affect the locations of underdense structures). In Lares et al. (2017), we show that the spatial locations of voids are correlated with voids with the same environment (void–in–void or void–in–cloud types) giving rise to void clumps. According to this study, clumps of R–type voids show a dynamical behaviour consistent with divergent flows, produced by a combination of mutually receding and expanding voids. On the other hand, clumps of S–type voids exhibit large–scale flows which are predominantly infalling

towards the clump centre. The global density of these clumps is, in most cases, positive. This implies that there must be overdense structures inside clumps which compensate the void underdensities. In reference to these ideas, we show in Fig. 1 a visualization of a FVS and its nearby voids for a subset in the simulation. We included A Visualization of a group of void–FVS pairs, including all the voids (represented as spheres) that have the FVS (in the center of the Figure) as their closest one. Arrows are scaled representations of the void velocity vector, with dotted segments located inside or behind voids. Other FVSs and voids in the neighbourhood are not shown for simplicity. In this context, we argue that large–scale flows play a key role in the formation of the supercluster–void network, and that superclusters might be responsible for the global collapse.

Here we focus on the relation between the positions and dynamics of voids relative to FVSs. The most common used statistic to quantify the relative distributions of two types of points is the two–point cross–correlation function, defined as the excess probability of finding a pair of objects at a given separation compared to that expected from a random distribution. However, neither voids nor FVSs can be easily represented by a point location. Voids are
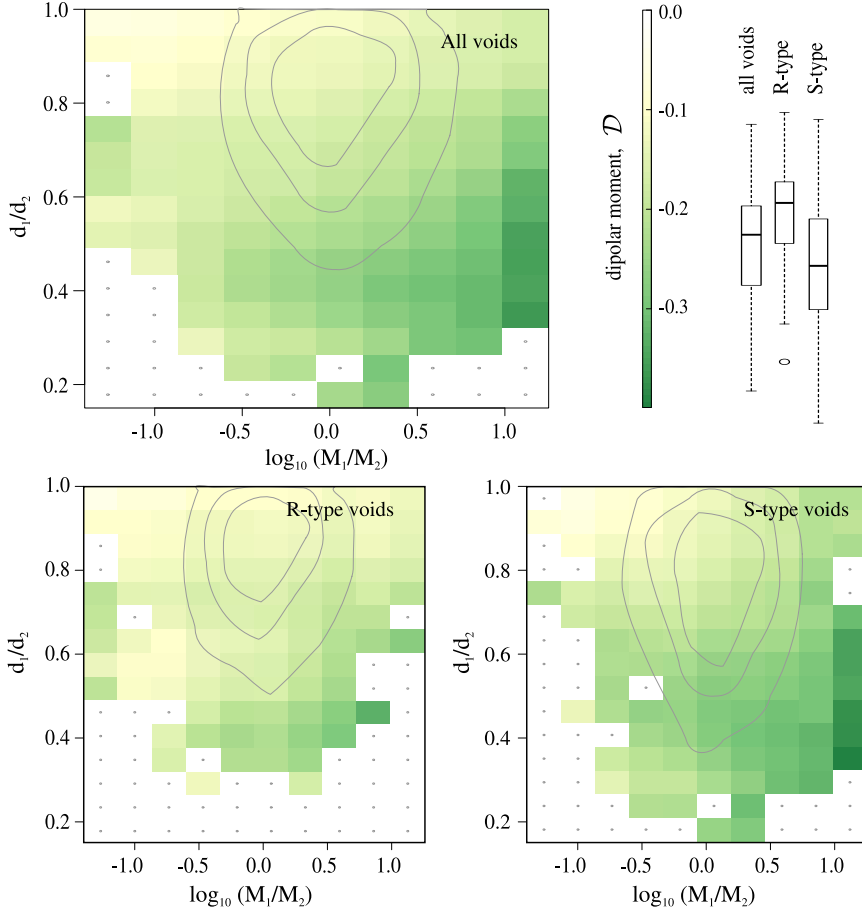
Figure 5. 2D histograms of the dipole moment estimator $\mathcal{D}$ for the distribution of $\cos(\theta)$, in bins of the ratios of masses and distances between the closest and the second closest FVS to each void. This estimator is computed for the closest void–FVS pair. Box plots and contour levels are analogous to those of Fig. 4.

characterized by a centre and a radius or scale. Moreover, FVSs do not have a simple shape and a centre can not be clearly defined.

We define a procedure to quantify the relative clustering of voids and FVSs as follows: if the locations of voids and FVSs are both random and independent, the probability for a randomly placed sphere of to be in contact with both types of structures should equal the product of the probability that the sphere touches a void times the probability of touching a FVS. These measures certainly depend on the size of the sphere, but if the distributions of the two types of structures are completely uncorrelated, the two probabilities are expected to be roughly the same. If, on the other hand, they are different, it would indicate a systematic tendency of either correlation (positive excess), or anticorrelation (negative excess) with respect to FVSs.

The previously introduced probabilities can be estimated using classical definitions, where the probability of a randomly placed sphere of being in contact with a void is approximated by the fraction of random spheres within the simulation box that contain at least a part of a void. The volume fraction occupied by the void is not relevant here, since this fraction can be studied as a function of the sphere radius. Then, if void ∩ FVS denotes the occurrence of a sphere that is in contact with both a void and a FVS,

$$P(\text{void} \cap \text{FVS}) \simeq \frac{N_{\text{void} \cap \text{FVS}}}{N_T}, \quad (1)$$

and similarly,

$$P(\text{void}) \simeq \frac{N_{\text{void}}}{N_T}, \quad (2)$$

$$P(\text{FVS}) \simeq \frac{N_{\text{FVS}}}{N_T}, \quad (3)$$

where N_V and N_{FVS} are the number of spheres that touch a void and a FVS, respectively. Also, notice that by definition, $P(\text{void} \cap \text{FVS}) = P(\text{void} \,|\, \text{FVS})\, P(\text{FVS})$. Then, it is equivalent to study $P(\text{void} \,|\, \text{FVS})$ as a function of $P(\text{void})$. In the upper panel of Fig. 2 we show these measures estimated as the fraction of spheres that touch simultaneously an FVS and a void, and the fraction of spheres that touch a void irrespective of FVSs. The upper curve correspond to S–type voids, and the lower curve to R–type voids, as indicated in the legends. The circles radii are proportional to the radius of the spheres, as indicated in the scale at the left. As it can be seen, there is a clear tendency of S–type voids to be located closer to FVSs than R–type voids. Indeed, if a random sphere contains a FVS, the probability of containing also an S–type void is higher than what should be expected for a random distribution of voids (represented by the dot-dashed line). Conversely, the probability that a FVS and an R–type void are in contact with the same random sphere is smaller in the full range of sphere radii, indicating that R–type voids tend to avoid FVSs. As the sizes of the spheres grow, the difference in probability with respect to the case of no void clustering decreases since any random sphere is likely to con-
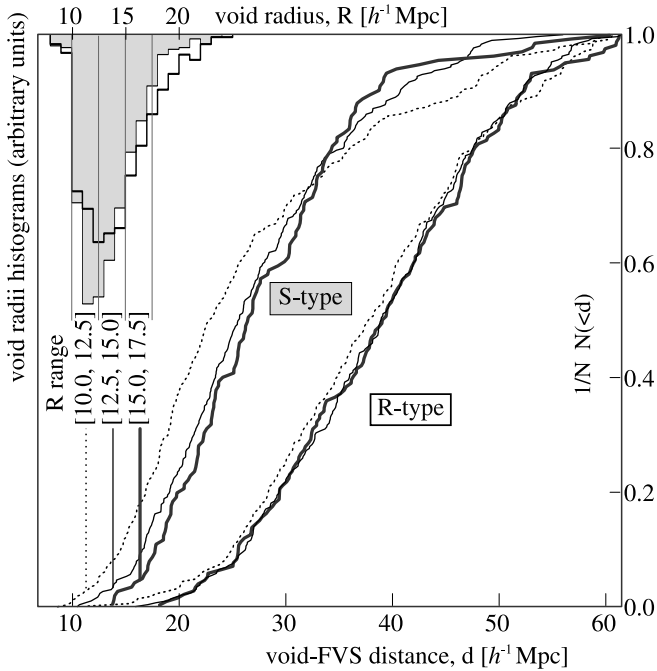
Figure 6. Cumulative distributions of void–FVS distances (bottom and right scales) for R/S–types and for different void radius intervals ($10.0 < R_v[h^{-1}\mathrm{Mpc}] < 12.5$ with dotted lines, $12.5 < R_v[h^{-1}\mathrm{Mpc}] < 15.0$ with thin solid lines, and $15.0 < R_v[h^{-1}\mathrm{Mpc}] < 17.5$ with thick solid lines). The histograms show the normalized distributions of void radii for R–types (empty bars), and S–types (filled bars). It can be clearly seen that the difference in the FVS–void distance cumulative distributions is dominated by void type and not by void size.

tain a FVS due to their large volume, and so the two probabilities become equivalent. From a scale of $\simeq 40 h^{-1}$ Mpc, no significant correlation signal can be detected. The probability excess can be writen as:

$$P(\mathrm{void}\,|\,\mathrm{FVS}) = P(\mathrm{void})\,(1 + \xi_{\mathrm{void-FVS}}(r)), \qquad (4)$$

for a given random sphere radius r.

In the bottom panel of this figure we show the void–FVS correlation function $\xi_{\mathrm{void-FVS}}(r)$ for S–type voids (upper curve, dashed line), R–type voids (bottom curve, solid line), and the combined sample of voids including both types (dotted line). It follows the definition of the correlation function given in Eq. 4. It is worth noticing that FVSs represent a small fraction of the total simulation box volume (nearly 4 per cent, see Luparello et al. (2011)) while voids comprise almost 20 per cent of the volume.

3.2 Dynamics of voids relative to FVSs

In the previous section we showed that there is a tight relation between the locations of voids of different types and the locations of FVSs. Moreover, this geometrical property in the distribution of the largest scale structures should also have a dynamical counterpart. The arguments presented in Sec. 1 suggest that the large–scale flows are closely related to the evolution of the largest scale structures, and consequently a dynamical connection between voids and FVSs is expected. Although the choice of the spherical approximation of voids is suitable, FVSs can not be described with simple geometrical objects, which implies that quantities such as relative
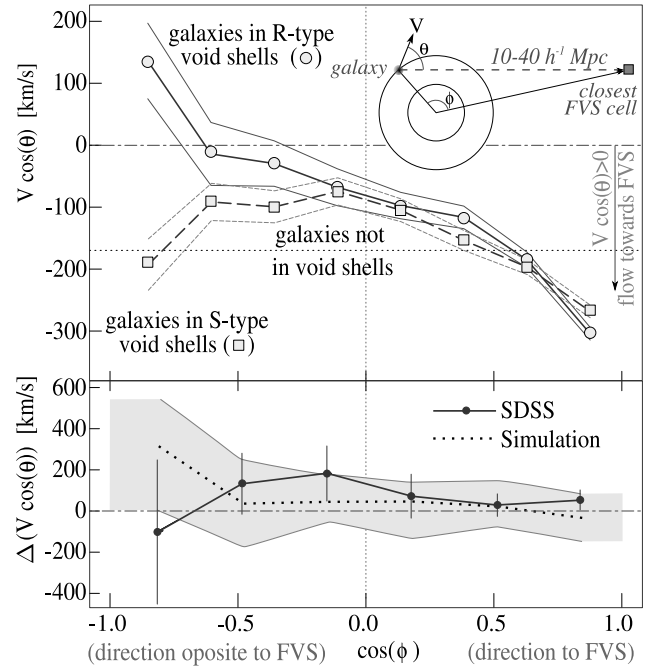

Figure 7. *Upper panel:* Mean projected velocity, V $\cos(\theta)$, for SAM central galaxies in void shells (solid lines:R–types, dashed lines: S–types) along the direction to the closest FVS as a function of the cosine of the angle ϕ between the position of the galaxy and the void centre–FVS direction. SAM galaxies outside voids are shown with an horizontal dotted line. *Bottom panel:* Velocity difference between galaxies in void shells of R/S types. The curves show the R−S velocity difference of galaxies in void shells projected onto the direction from the void centre to the FVS, as a function of cos (ϕ). The angle ϕ gives the relative position of the galaxies with respect to the FVS direction and is shown in the scheme of the upper panel. The thick solid line gives the results for SDSS data, with uncertainties computed through Jackknife resampling. The dotted line corresponds to the simulation. The uncertainty region provides a 2–σ measure of cosmic variance associated with the SDSS volume.

distance, position or velocity between those two types of structures are not straightforward to compute.

Here, we adopt a simple approach that takes into account basic dynamical principles and allows to study the joint dynamical behaviour of voids and FVSs. To analyse the dynamic of FVS–void pairs, as the first step we identify the nearest FVS for each void. Since the FVSs have complex shapes, we consider the core region of each FVS, defined as the volume covered by the highest density cells. As we mentioned in Sec. 2.3, in the identification of these structures we have used a physically motivated threshold on luminosity overdensity (Luparello et al. 2011), following the criteria calibrated on simulations by Dünner et al. (2006). According to this procedure, we chose a ratio of luminosity density, ρ_{lum}, relative to the mean satisfying $\rho_{\mathrm{lum}}\,/\,\bar{\rho}_{\mathrm{lum}} > 5.5$ to define the boundaries of a FVS in a 3D grid–averaged smoothed density field estimation. Thus, since the densest region of the FVSs roughly match the central region, we define as the central, denser component of a FVS all cells having $\rho_{\mathrm{lum}}\,/\,\bar{\rho}_{\mathrm{lum}} > 6.3$ (corresponding to the median of the luminosity density distribution of FVS cells). The distance between a void and a FVS is then defined as the distance between the void centre and the closest cell of the densest core of the FVS. For each of the closest void–FVS pair we compute their relative position and velocity. To this aim, we define the velocity of the closest

FVS cell as the average of the velocities of the galaxies inside a sphere centred in the high density cell and with radius equal to the distance between the void centre and this cell. The void velocity is then taken relative to their corresponding closest high density cell. The angle between these relative position and velocity vectors, θ, allows to study the flow onto FVSs.

In order to characterize the void–FVS relative motions, we consider the preference of relative void velocity vectors towards the direction to FVSs. We quantify this coherence by means of a dipole moment estimation, $\mathcal{D}$, calculated as the average over all void–FVS pairs of the values of $\cos(\theta)$, weighted by the second order Legendre polynomial $P_2(x)$ evaluated in $x = \cos(\theta)$:

$$\mathcal{D} = \frac{1}{N} \sum_{i=1}^{N} \cos(\theta)\, P_2\big(\cos(\theta)\big) \qquad (5)$$

It could be argued that S–type voids close to FVSs are likely to show a stronger infall towards FVS than R-type voids since these are located more distantly. To test this hypothesis, we have performed a preliminary analysis by selecting two subsamples of void–FVS pairs: one comprising only S–type voids close to a luminous FVS and the other, only by R–type voids far from low luminosity FVSs. The results for these subsamples, shown in the histograms of Fig. 3, are consistent with a significant infall pattern of S–types and a lack of coherence of R–types. In order to visualize how the computed dipole values characterize the relative infall/outflow patterns, in the inset on top of the figure we show model distributions of $\cos(\theta)$ with a purely dipole component. The scheme in this figure is consistent with distributions of $\cos(\phi)$ dominated by negative values representing an infall pattern flowing towards FVS. We explored the magnitude of the dipole moment as a function of the relative distance between the void and the FVS, the mass of the nearest FVS, the mass ratio between the first and second nearest FVSs, and the distance ratio between the first and second nearest FVSs.

In the upper panel of Fig. 4 we show the dipole moment $\mathcal{D}$ of the $\cos(\theta)$ distributions in bins of FVS mass M_1 and void–FVS distance d_1. As it is shown in this figure, the higher negative values of the dipole (that indicates an infall signal for the pairs) occurs mainly when the voids are located close to a FVS. This statistical excess is significant even at distances as large as $50h^{-1}$ Mpc. However, it is important to note that besides the low number of objects, the higher values of $\mathcal{D}$ correspond to the most massive FVSs. In grey we show the level curves of the number of pairs FVS–void which correspond to the 25, 50 and 75 per cent of the sample. White bins, with a central dot, do not contain any pair. For the rest of the matrix, we applied a smoothing kernel using a top–hat window of 2 bins each side (ignoring empty bins). The color scale indicates the values of the $\mathcal{D}$ statistic defined in Eq. (5). The limits of this scale are the same as the color scale in Fig. 3, that gives a picture of the degree of anisotropy that correspond to the different values of the $\mathcal{D}$ statistic. In left and right lower panels of Fig. 4 we show the dipole moment for R–type and S–type voids, respectively. Box plots correspond to the distributions of $\mathcal{D}$ for each sample. There is a stronger infall signal for S–type voids, which is noticeable up to nearly $25h^{-1}$ Mpc of void–FVS separation. Also, in agreement with the results of the previous section, it can be noticed that S–type voids tend to be located closer to superstructures than R–type voids.

However, these results are obtained taking into account only the nearest FVS to each void. The possible presence of other structures at similar distances lead us to take into account the influence of at least the second nearest structure. To this aim, we compute the relative distance between the void and their nearest FVS (d_1) and the void and their second nearest FVS (d_2), and the ratio of the corresponding FVSs distances and masses. Following the same scheme of Fig. 4, in Fig. 5 we show the dipole moment as a function of the relative distances and masses. The data shown in these figures are not exactly the same due to different mass and distance limits, which produce slightly diferent box plots. Here, we can see that if the nearest FVS is remarkably closer to the void there is a clear infall signal, and this intensifies if the nearest FVS is much more massive than the second one. In this figure we distinguish R– and S–types showing S–type voids preferentially located closer to their nearest superstructure. In Fig. 6 we show the cumulative distributions of void–FVS distances (bottom and right scales) for R/S–types and for different void radius intervals ($10.0 < R_v/(\mathrm{Mpc\,h}^{-1}) < 12.5$ with dotted lines, $12.5 < R_v/(Mpc\,h^{-1}) < 15.0$ with thin solid lines, and $15.0 < R_v/(Mpc\,h^{-1}) < 17.5$ with thick solid lines). The histograms show the distributions of void radii for the two void types (upper scale, with arbitrary normalization), with filled bars for S–types and empty bars for R–types. The shift in the cumulative distributions are larger considering void type, indicating that it is not dominated by void size segregation. Also, in S–type voids we can see that the infall signal grows when the mass of their nearest FVS (M_1) is greater than the mass of the second one (M_2).

3.3 Galaxies in void shells

In order to study the influence of the large–scale flows on galaxies we analyse the velocity field related to the spatial configuration of the systems. To this aim we use SAM central galaxies and identify their nearest FVS to calculate their relative projected velocity. Our sample comprises 79403 galaxies, out of which 1996 are located in R–void shells and 3364 in S–void shells. We also distinguish between galaxies located in void shells or elsewhere and we restrict to galaxy–FVS distances in the range $10 - 40h^{-1}$ Mpc. In the upper panel of Fig. 7 we show the mean projected velocity, $V \cos(\theta)$, of galaxies in void shells as a function of their relative angle, ϕ, with respect to the direction that connects the void centre and the nearest FVS, as outlined in the scheme. The location of a galaxy in the void shell with respect to the FVS direction is given by $\cos(\phi)$. Galaxies in the cap facing the FVS have $\cos(\phi) > 0$, and galaxies opposite to the FVS, $\cos(\phi) < 0$, as indicated in the figure axis. We use a sign convention where negative values of $V \cos(\theta)$ correspond to galaxies that are moving towards the FVS. Negative values of $\cos(\phi)$ correspond to a galaxy–void–FVS configuration (as in scheme), while positive values to void–galaxy–FVS. It should be noticed that we are using the densest cells in the FVS definition, so that the cell in the scheme represents the closest cell in the subset $\rho_{\mathrm{lum}} / \bar{\rho}_{\mathrm{lum}} > 6.3$. It can be appreciated in this figure that galaxies in R–type void shells may overcome the infall of the void onto the FVS when the galaxies are located in the direction opposite to the superstructure. When galaxies are facing directly to the superstructure, they exhibit the same infall pattern, irrespective of residing in R– or S–type void shells. We notice that this infall is stronger than that of galaxies elsewhere at the same galaxy–FVS distance due to void dynamics.

4 OBSERVATIONAL RESULTS

In this section we analyse spatial correlations and dynamics of voids and FVSs for data in the SDSS catalogue. As in Fig. 2, we
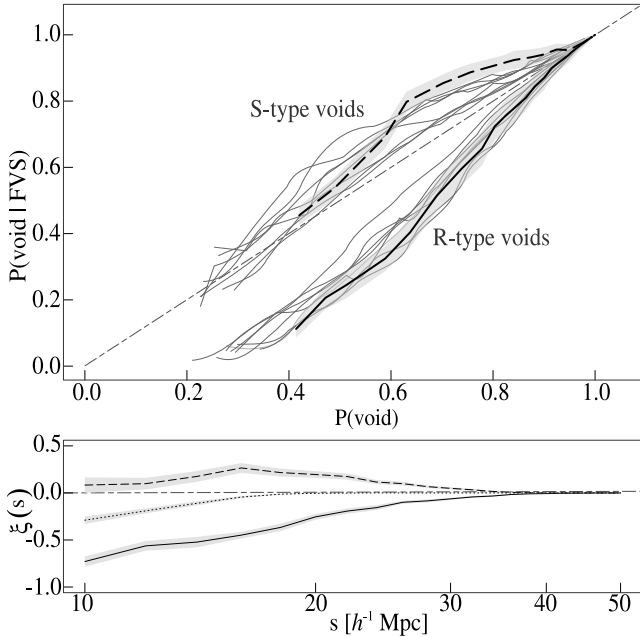
Figure 8. Spatial distribution of voids with respect to FVSs, in the SDSS data. Upper panel: Conditional probability of finding a randomly placed sphere containing void and FVS volume fractions simultaneously, $P(\text{void} \mid \text{FVS})$ as a function of the probability that the same sphere contains a fraction of void volume $P(\text{void})$. The shaded regions indicate Jackknife resampling uncertainties. The grey curves correspond to random regions within the simulation with the same volume than SDSS sample. The bottom panel show the corresponding void–FVS correlations, in a similar way to Fig. 2.

show in the upper panel of Fig. 8 the conditional probability of finding a randomly placed sphere that jointly contain parts of FVSs and voids of S– (upper curves) or R–types (lower curves), as a function of the probability that a sphere of the same size contacts at least part of voids. We remark the good agreement between observations and the simulation (Fig. 2), in spite of the fact that the observational results correspond to redshift space measurements, due to the large distances involved. Since the volume of the SDSS data is much smaller than the volume of the simulation, we computed the quantities previously defined in Eqs. 1 to 4, in regions of the simulation with the same SDSS volume. We show with grey curves the corresponding relations for eight independent regions in the simulation box. The spread of these curves as a function of $P(void)$ allows a judgement of the cosmic variance that affects the calculation of the probabilities. The grey shaded regions around black curves are the Jackknife uncertainties for the data. In the bottom panel of this figure we show the corresponding void–FVS correlation function for SDSS data. As it can be seen, the results obtained for SDSS data are consistent with those of the simulation. We find that the same general trends obtained in the full simulation box (Fig. 2) are suitably reproduced for SDSS data.

In Fig. 9 we show the histograms of $\cos(\theta)$ in four subsamples to show the effects of mass and distance to the closest FVSs. For reference, we show the corresponding values of the dipole moment $\mathcal{D}$ which should be considered in the context of Fig. 5, that gives the same analysis in the simulation taking advantage of the larger statistics. In panel (a), we show voids located at a distance to the closest FVS, smaller than 60 per cent of the distance to the

second closest FVS satisfying a total luminosity ratio of at least 0.6. These restrictions take into account the results shown in Fig. 5 for the simulation box, and corresponds to the bottom–right corner, where the dipole moment signal has the larger amplitude. In this case there is a clear prevalence of negative values of $\cos(\theta)$, which is consistent with a negative value of the dipole moment. In panel (b) we show the histogram of $\cos(\theta)$ for voids closer than $20h^{-1}$ Mpc to FVSs that have a total luminosity of at least $10^{13} L_\odot$. Similarly to the previous subsample, this region is selected from the upper panel of Fig. 4 corresponding to the bottom–right corner of the plot. We also considered two additional restrictions corresponding to voids closer than $20h^{-1}$ Mpc to FVSs and a total luminosity up to $10^{13} L_\odot$ (in panel (c) of Fig. 9), and to voids associated with luminous FVSs ($L > 10^{13} L_\odot$) separated by a distance greater than $30h^{-1}$ Mpc (panel (d)). This limiting mass was chosen so that the signal to noise ratio is high, and taking into account the results in the simulation (Fig. 4) that indicate that more massive FVSs have a more noticeable dipole moment. We argue that the infall patterns observed in the simulation box are also reproduced in the SDSS data, despite its much smaller volume and the linearized velocity field approximation.

In the bottom panel of the Fig. 7 we show the velocity pattern for the infall of galaxy groups in void shells onto FVSs. Our sample comprise 189 and 293 groups in R– and S–type void shells, respectively, in the $10 - 40h^{-1}$ Mpc galaxy–FVS distance range. The curves show the projected R-S velocity difference of groups in void shells onto the direction from the void centre to the FVS as a function of the location of the group. The angle ϕ between the relative position of the group and the FVS direction is as indicated in the scheme of the Fig. 7. The dotted line is the resulting difference for the simulation. The solid line corresponds to SDSS data, with error bar indicating Jackknife resampling uncertainties. The region around the curve of the simulation gives an estimation of cosmic variance in order to compare to observations. It is computed from many randomly placed regions within the simulation with the same volume than SDSS data, and corresponds to a 2-σ uncertainty.

5   DISCUSSION

In this work we have explored the void–superstructure spatial cross–correlations and their influence on the large–scale velocity flows. To this end, we have studied the velocity field associated with galaxies in void shells to deepen our understanding of the supercluster–void network evolution.

Our void and superstructure catalogues are defined according to Ruiz et al. (2015) and Luparello et al. (2011), respectively. Therefore, voids correspond to spherical regions with integrated total density of 10 percent the mean value up the void radius, and superstructures are derived from a smoothed luminosity field that isolates the highest density regions. These two definitions rely on physical grounds, namely the void sample has a constant integrated tracer density within void radii, and superstructures correspond to future virialized systems in the acelerating Λ cold dark matter scenario.

In order to study the spatial correlations between voids and superstructures, we defined a modified version of the correlation which is usually applied to point data. This allows to measure the tendency of voids to be located at a given distance from a superstructure and detect if they are preferentially located near FVSs or avoiding them. We find that while voids–in–clouds (S–types) are preferentially located near superstructures, voids–in–voids (R–
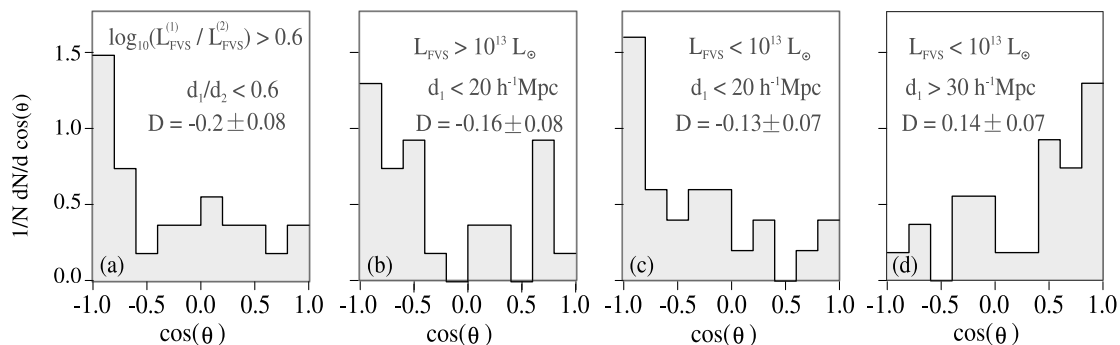
Figure 9. Histograms of the $\cos(\theta)$ for different samples of voids in SDSS. (a) Voids that are at a distance to the closest FVS smaller than 60 per cent of the distance to the second closest FVS, and also satisfying the ratio of the total luminosities of the two closest FVS > 0.6, (b) Voids closer than 20 h^{-1} Mpc to FVSs having a total luminosity of at least 10^{13} $L_\odot$, (c) Voids closer than 20 h^{-1} Mpc to FVSs having a total luminosity up to 10^{13} $L_\odot$, and (d) Voids near FVSs with $L < 10^{13}$ $L_\odot$ separated by a distance greater than 30 h^{-1} Mpc. We show the values of the dipole moments corresponding to each panel, with bootstrap resampling error estimates.

types) are likely to avoid them. This is somewhat related to the selection of voids according to their environment, but we find that it has also dynamical implications when considered in the context of the large–scale structure, manifested on the infall of voids which are close to FVS independently of void type.

We also explored galaxies in void shells and how the presence of a nearby superstructure affects its dynamics. Galaxies in S– and R–type void shells within 40 h^{-1} Mpc infall onto superstructures except for galaxies opposite to superstructures in R–type void shells. Moreover, we find a stronger infall for galaxies residing in void shells facing the closest superstructure than galaxies at the same relative distance elsewhere. We have analysed the similarity of the simulation results and those inferred from the SDSS galaxy catalogue. In spite of the SDDS smaller observational volume and linear velocity approach, and the fact that the Millenium simulation cosmological parameters differ from more recent observational estimates (Planck Collaboration et al. 2016), the general trend agreement is encouraging.

Large–scale flows may be analysed into different contexts. (see for instance Shandarin 2011; Shandarin et al. 2012; Cautun et al. 2014, and references therein). In our study, galaxy motions in void shells can be thought as a combination of shell expansion (Paz et al. 2013), void bulk motion (Lambas et al. 2016) and the infall onto superstructures (this work). The magnitude of these effects are comparable and need to be taken into account in simple models for galaxy motions. Our findings go along with the scenario proposed by Tully et al. (2008) and Tully et al. (2014) where the presence of underdense regions contribute significantly to the velocity flow of galaxies in the local universe.

ACKNOWLEDGEMENTS

REFERENCES

Abazajian K. N., et al., 2009, ApJS, 182, 543
Aragón-Calvo M. A., Platen E., van de Weygaert R., Szalay A. S., 2010, ApJ, 723, 364
Cautun M., van de Weygaert R., Jones B. J. T., Frenk C. S., 2014, MNRAS, 441, 2923
Ceccarelli L., Padilla N. D., Valotto C., Lambas D. G., 2006, MNRAS, 373, 1440
Ceccarelli L., Paz D., Lares M., Padilla N., Lambas D. G., 2013, MNRAS, 434, 1435
Ceccarelli L., Ruiz A. N., Lares M., Paz D. J., Maldonado V. E., Luparello H. E., Garcia Lambas D., 2016, MNRAS, 461, 4013
Contreras S., Baugh C. M., Norberg P., Padilla N., 2013, MNRAS, 432, 2717
Contreras S., Baugh C. M., Norberg P., Padilla N., 2015, MNRAS, 452, 1861
Dünner R., Araya P. A., Meza A., Reisenegger A., 2006, MNRAS, 366, 803
Einasto J., Saar E., Klypin A. A., 1986, MNRAS, 219, 457
Einasto J., Einasto M., Frisch P., Gottlober S., Muller V., Saar V., Starobinsky A. A., Tucker D., 1997, MNRAS, 289, 813
Einasto J., et al., 2011, A&A, 534, A128

Guo Q., et al., 2011, MNRAS, 413, 101

Hahn O., Carollo C. M., Porciani C., Dekel A., 2007, MNRAS, 381, 41

Lambas D. G., Lares M., Ceccarelli L., Ruiz A. N., Paz D. J., Maldonado V. E., Luparello H. E., 2016, MNRAS, 455, L99

Lares M., Ruiz A., Luparello H., Ceccarelli L., Garcia Lambas D., Paz D. J., 2017, MNRAS, 468, 4822

Leclercq F., Jasche J., Wandelt B., 2015, J. Cosmology Astropart. Phys., 6, 15

Luparello H., Lares M., Lambas D. G., Padilla N., 2011, MNRAS, 415, 964

Padilla N. D., Ceccarelli L., Lambas D. G., 2005, MNRAS, 363, 977

Paranjape A., Lam T. Y., Sheth R. K., 2012, MNRAS, 420, 1648

Paz D., Lares M., Ceccarelli L., Padilla N., Lambas D. G., 2013, MNRAS, 436, 3480

Planck Collaboration et al., 2016, A&A, 594, A13

Platen E., van de Weygaert R., Jones B. J. T., 2008, MNRAS, 387, 128

Ruiz A. N., Paz D. J., Lares M., Luparello H. E., Ceccarelli L., Lambas D. G., 2015, MNRAS, 448, 1471

Shandarin S. F., 2011, J. Cosmol. Astropart. Phys., 2011, 015

Shandarin S., Habib S., Heitmann K., 2012, Phys. Rev. D, 85, 083005

Sheth R. K., van de Weygaert R., 2004, MNRAS, 350, 517

Spergel D. N., et al., 2003, ApJS, 148, 175

Springel V., et al., 2005, Nature, 435, 629

Tully R. B., Shaya E. J., Karachentsev I. D., Courtois H. M., Kocevski D. D., Rizzi L., Peel A., 2008, ApJ, 676, 184

Tully R. B., Courtois H., Hoffman Y., Pomarède D., 2014, Nature, 513, 71

Van de Weygaert R., Platen E., 2011, International Journal of Modern Physics: Conference Series, 01, 41

Wang H., Mo H. J., Jing Y. P., Guo Y., van den Bosch F. C., Yang X., 2009, MNRAS, 394, 398

Wang H., Mo H. J., Yang X., van den Bosch F. C., 2012, MNRAS, 420, 1809

Yang X., Mo H. J., van den Bosch F. C., Jing Y. P., 2005, MNRAS, 356, 1293

Yang X., Mo H. J., van den Bosch F. C., Pasquali A., Li C., Barden M., 2007, ApJ, 671, 153

van de Weygaert R., 2016, in van de Weygaert R., Shandarin S., Saar E., Einasto J., eds, IAU Symposium Vol. 308, The Zeldovich Universe: Genesis and Growth of the Cosmic Web. pp 493–523 (arXiv:1611.01222), doi:10.1017/S1743921316010504